Article

In Vitro Bioactivity and Cell Biocompatibility of a Hypereutectic Bioceramic

Patricia Mazón [1],* **, Patricia Ros-Tárraga [2]** **, Sara Serena [3], Luis Meseguer-Olmo [4]**
and Piedad N. De Aza [5]

[1]   Departamento de Materiales, Óptica y Tecnología Electrónica, Universidad Miguel Hernández,
     Avda Universidad s/n, Elche (Alicante) 03202, Spain

[2]   Grupo de Investigación en Regeneración y Reparación de Tejidos, UCAM-Universidad Católica San Antonio
     de Murcia, Guadalupe, Murcia 30107, Spain; p.ros.tarraga@gmail.com

[3]   Instituto de Cerámica y Vidrio, CSIC, 28049-Cantoblanco, 28049 Madrid, Spain; serena@icv.csic.es

[4]   Service of Orthopaedic at Arrixaca University Hospital, UCAM-Catholic University of Murcia,
     30120 Murcia, Spain; lmeseguer.doc@gmail.com

[5]   Instituto de Bioingeniería, Universidad Miguel Hernández, Avda Ferrocarril s/n,
     03202 Elche (Alicante), Spain; piedad@umh.es

*   Correspondence: pmazon@umh.es; Tel.: +34-96-6658624; Fax: +34-96-5222033

check for
updates

Abstract: Two dense biphasic ceramics, with a hypereutectic composition of 30 wt % $CaSiO_3$–70 wt % $Ca_3(PO_4)_2$, were synthesized by a solid-state reaction of homogeneous pressed combinations of previously synthesized synthetic $CaSiO_3$ and $Ca_3(PO_4)_2$ powders. The objective was to produce a dense structure to generate large enough in situ pores for the ceramic to be used in tissue engineering. To develop such a structure, two grain sizes of $CaSiO_3$ were used (63–100 μm and 100–150 μm) and some of their properties were studied in vitro, as they are relevant for tissue engineering. X-ray diffraction analysis, μ-Raman spectroscopy, diametrical compression test, and scanning electron microscopy with elemental mapping showed a coarse-grained homogeneous microstructure for the materials, which consisted of wollastonite (α-$CaSiO_3$) and tricalcium phosphate (α-$Ca_3(PO4)_2$), with adequate mechanical properties for implantation. In vitro bioactivity was evaluated in simulated body fluid (SBF) by exploring a hydroxyapatite (HA)-like formation. The results showed that tricalcium phosphate grains dissolved more preferentially than those of wollastonite, but not fast enough to leave a pore before the surface was coated with an HA-like layer after soaking only for three days. Biocompatibility was evaluated by in vitro cell experiments, which showed cell proliferation, adhesion, and spreading on the ceramic surface. This ceramic is expected to be used as a bone graft substitute.

Keywords: hypereutectic; scaffold; bioceramics

1. Introduction

Continuous human evolution related with materials and technology has led to major improvements, such as considerable prolonged human life expectancy. Some consequences from such development are related with diseases of an ageing population or injuries from trauma accidents, which render strategies to repair, replace, and even regenerate damaged osseous tissue necessary. Tissue engineering researches new biomaterials that could meet these demands. In this group of materials, ceramics have received more attention given their good properties: for example, their ability to favor bone adhesion and bone ingrowth when implanted into animal and human bodies. The use of calcium phosphates is very popular because their compositions are similar to the mineral bone

part [1,2], but P_2O_5-free calcium silicates have also been able to develop a hydroxyapatite layer on their surfaces [3,4], which is key to bone–implant interactions.

The success of a biomaterial to be used as an implant is related not only to its intrinsic properties but also to the required hierarchical structure. In addition to surface connections to bone tissue, it must act as a temporary template by stimulating and guiding bone natural regeneration, and it degrades at a rate that guarantees mechanical support [5]. The porous structure has been developed by different methods, such as the polymeric sponge method, the use of porogens, foaming techniques, 3D printing, and so on [6–9]. Although there is some controversy as to the ideal pore size [10–12], it is clear that interconnection and the macro- and microporosity combination are critical factors to gain scaffolds capable of mimicking cancellous bone.

Another goal to achieve with this porous structure is to maintain mechanical support in the early bone regeneration stage. A good approach to overcome this problem has been devised by De Aza et al. by the in situ generation of a porous template by soaking a biphasic ceramic of $CaSiO_3$ (W)-$Ca_3(PO_4)_2$ (C_3P) of a eutectic composition in simulated body fluid (SBF), and by the dissolution and transformation of a dense ceramic into a porous one [13,14]. Nevertheless, when the ceramic was implanted in vivo, transformation only took place on the surface of the material at a depth of 200 μm because the pores left by the dissolution of the W phase in the eutectic structure were very narrow (~1.5 μm). Thus bone tissue was unable to completely osteointegrate the implant [15].

However, by means of processing, it is possible in material science to adapt the bioceramic potential implant size, shape, and microstructure. To overcome this problem, in the present work we studied a hypereutectic composition that was rich in $Ca_3(PO_4)_2$ (the phase in which the material with a eutectic composition transforms pseudomorphically into hydroxyapatite (HA) after soaking in SBF) and with two grain sizes of $CaSiO_3$ powder because it is the biodegradable phase [16]. We hypothesized that the new ceramic would develop in situ a structure with large enough pores for cells to colonize it completely and would consequently present total implant osteointegration in vivo.

In order to check our initial hypothesis, the new hypereutectic ceramic was tested in vitro in SBF. Adult human mesenchymal stem cells (*ah*MSCs) were used to study their interaction and biological response when in contact with the prepared ceramics to study their biocompatibility, attachment, adhesion, and proliferation.

2. Materials and Methods

2.1 Materials Preparation

The starting material included laboratory wollastonite and tricalcium phosphate synthesized by a solid-state reaction according to a procedure described in a previous study [17,18]. C_3P was milled in an attrition mill for 3 min using isopropanol and 20 mm diameter PSZ-zirconia balls. The obtained powder was dried at 60 °C/24 h and sieved through a 30 μm mesh.

The W material was ground in a tungsten carbide mill and sieved. The powder that was left in sieves between 63–100 μm and 100–150 μm was chosen to prepare the two ceramics.

The hypereutectic ceramic materials were prepared by a mixture of W and C_3P at a ratio of 30:70 wt %, referred to hereafter as W-C_3P 1 (63–100 μm of W) and W-C_3P 2 (100–150 μm of W). The mixture was homogenized with acetone, and pressed into bars (~7 mm ⌀ × 80 mm long), with isostatic pression at 200 MPa to form green compacts.

Green compacts were sintered at 1325, 1350, and 1375 °C/6 h in air at heating and cooling rates of 5 °C/min to determine the optimum sintering temperature. From the sintered bars, diamond machining was performed for the prepared characterization.

2.1. Ceramics Characterization

In order to study the densification degree of the sintered hypereutectic ceramics, bulk density was performed using Archimedes´s method and porosity by mercury porosimetry (Poremaster-60

GT, Quantachmore Inst., Boyton Beach, FL, USA). Five samples for each sintering temperature were studied and standard deviation was calculated.

X-ray diffraction (XRD) was used for the mineralogical analysis done on the 120 μm powder samples. A Bruker AXS D8-Advance powder X-ray diffractometer (Karlsruhe, Germany) by λCuKα1 radiation (1.5418 Å) and a secondary curved graphite monochromator were used for obtaining XRD patterns. Standards from the Joint Committee on Powder Diffraction Standards (JCPDS) database were used as a reference in relation to the obtained diffractograms, α-C_3P (JCPD-09-0348) and α-$CaSiO_3$ (JCPD-74-0874).

Confocal Raman measurements were taken using a 532 nm excitation laser (green laser) and a 20X objective lens. Raman spectra were recorded within a spectral range, which went from 100 to 1200 cm^{-1}, and were analyzed by the Witec Control Plus software (Witec alpha − 300R, Witec, Ulm, Germany).

The obtained ceramic materials were embedded in a vacuum in an epoxy resin and were then progressively polished down to 0.1 μm by diamond paste and etched with acetic acid (1% concentration, 10 s). Ultrasonic bath with distilled water was used for cleaning and, after drying, they were palladium-coated for scanning electron microscopy (SEM, Hitachi S-3500N, Ibaraki, Japan), including a wavelength dispersive spectroscopy system (WDS, INCA-Oxford, UK).

A Zeta-20 3D imaging and metrology microscope (Zeta-20 Optical Profilometer, Zeta Instruments, San Jose, CA, EEUU) was used to acquire the height data presented herein. The 3D images of the surface texture were acquired at the 50X optical magnification.

The mechanical properties of the bioceramics were studied using the Brazilian test, namely, the diametrical compression of discs test (DCDT). Circular discs were used with a ratio diameter/thickness (D/T) of ~0.3, and they were placed between two stainless steel loading plates with their faces perpendicular to the loading plates in a universal testing machine (Microtest, Spain) The load was applied with a displacement rate of 5 mm/min until the sample cracked. Fifteen specimens of WTCP 1 were tested as representative one, and strength was calculated using Equation (1):

$$\sigma = 2P/\pi DT \tag{1}$$

where P is the applied load, D is the diameter, and T is the thickness of the disc.

For brittle materials, the weakest link theory [19] was applied to analyze the distribution of strength values. The Weibull parameters were determined using the ENV-843-5 procedure through the Weibull function represented in Equation (2):

$$P_f(\sigma) = 1 - \exp\left(-\sigma^m/\sigma_0^m\right) \tag{2}$$

where $P_f(\sigma)$ is the failure probability, σ_0 is the strength (failure probability 63.2%), and m is the Weibull modulus.

According to this standard, the probabilities of failure were calculated using Equation (3):

$$P_f = (n - 0.5)/N \tag{3}$$

where N is the total number of specimens tested and n is the specimen rank in ascending order of failure stress.

2.2. SBF Test

An in vitro bioactivity analysis was done according to Kokubo's protocol [20]. The ceramic bars obtained after thermal treatment were cut as discs (7 mm in diameter, 1.5 mm thickness). Polystyrene bottles were used to immerse the discs hooked onto a nylon thread in SBF (50 ml), which has an ion concentration that is almost equal to human blood plasma, pH = 7.4. The samples immersed in the bottles with SBF were shaken in a water bath at 37 °C for pre-established periods of time. After the corresponding soaking period (up to four weeks), samples were removed from SBF, rinsed with

deionized water, and dried at room temperature. Sample surfaces and cross-sections were examined by SEM and a microanalysis by WDS. For the cross-section analysis, 10 measures per sample were taken in five samples. The silicon, calcium, and phosphorus ion release profiles were determined for all the samples studied by inductively coupled plasma optical omission spectroscopy (ICP-OES, Perkin Elmer Optima 2000^{TM}, PerkinElmer Inc., Waltham, MA, USA).

For the transmission electron microscopy (TEM, JEM-2010 JEOL, Tokio, Japan) study, the precipitated layer on the scaffold's surface was carefully removed using a razor blade and dispersed on the surface of a Petri dish with ethanol. After drying, a powder specimen was collected on a carbon-coated TEM copper grid (300 mesh). Electron beam transparent particles were chosen for the TEM examination by selected area diffraction (SAD).

2.3. Biocompatibility, Adhesion, and Proliferation Assays

The *ah*MSCs used for the study were isolated as previously described [21] according to the International Society of Cell Therapy (ISCT) criteria [22] for their characterization. The assays were approved by the Institutional Ethical and Clinical Trials Committee (V. Arrixaca University Hospital of Murcia). Informed consents were obtained from all the volunteers.

The *ah*MSCs of third passage (P3), after cell expansion, were prepared for use in all the cellular studies. Biocompatibility, adhesion, and proliferation studies were performed by seeding a density of 5000 cells/cm^2 of *ah*MSCs on top of the W-C$_3$P 2 ceramics, which had been previously pre-incubated for 24 h with 500 μL of fetal bovine serum (FBS), and placed in 48-well culture plates with 500 μL of growth medium (GM) which consisted of Dulbecco's Modified Eagle Medium (DMEM) with 10 % of FBS and 1 % penicillin-streptomycin (all from Sigma-Aldrich, St. Louis, MO, USA). All the samples were incubated at 37 °C in a 5 % CO$_2$ atmosphere with 95 % relatively humidity. Medium was changed every three to four days.

Field emission scanning electron microscopy (FESEM, Merlin VP Compact, Carl Zeiss Microscopy S.L., Oberkochen, Germany) was used to examine cell adherence growth and morphology at 1, 7, 14, 21, and 28 days in GM.

2.4. Cell Viability Assay

The reagent Alamar Blue (Invitrogen, Carlsbad, CA, USA) is non-radioactive, safe, and stable in environment assays. This was why it was used to measure the cellular well-being and viability of *ah*MSCs on the W-C$_3$P 2 surface. The top of the samples was seeded with 5000 cells/cm^2 in a 48-well plate and incubated under the same conditions described above for 1, 7, 14, 21, and 28 days with GM.

Medium was replaced every three days and a positive control was also used by seeding *ah*MSC onto tissue-treated polystyrene (TCPS) culture plates. When each culture period ended, the corresponding medium was discarded and wells were washed twice with phosphate buffer solution (PBS). Each well was then filled with 500 μL of fresh medium containing 10 % (*v/v*) of Alamar Blue reagent to be incubated at 37 °C for 4 h. After the reaction time, 200 μL of dissolution were transferred to a 96-well plate and the fluorescence analysis was carried out directly in a Synergy MX ultraviolet visible (UV-Vis) reader (BioTek Instruments Inc., Winooski, VT, USA) at excitation and emission wavelengths of 560 nm and 590 nm, respectively. The results are reported as arbitrary units (a.u.)

All the experiments were performed at least in triplicate. Student's *t*-test (*p*-value <0.05), was used in case of any possible significant differences between groups. All the data are reported as mean ± standard deviation (SD).

3. Results

3.1. Biomaterial Characterization

A summary of the microstructural parameters of the ceramic results are shown in Table 1. The maximum level of shrinkage corresponded to 1375 °C, which reached a much higher value for the

ceramic with the biggest W grain size. The maximum apparent density values also corresponded to the maximum sintering temperature for both ceramics. As well as the minimum porosity, the minimum values corresponded to a higher sintering temperature, but, in this case, no significance difference was observed between both ceramics.

Table 1. Microstructural parameters of the ceramics.

Parameters	W-C$_3$P 1			W-C$_3$P 2		
Temperature (°C)	1325	1350	1375	1325	1350	1375
Shrinkage (%)	15.3 ± 0.5	18.4 ± 0.5	22.1 ± 0.5	18.7 ± 0.5	19.2 ± 0.5	23.0 ± 0.5
Apparent density (gr/cm^3)	2.55 ± 0.05	2.71 ± 0.05	3.10 ± 0.05	2.58 ± 0.05	2.83 ± 0.05	3.17 ± 0.05
Porosity (%)	3.7 ± 0.2	2.6 ± 0.2	1.5 ± 0.2	3.4 ± 0.2	2.8 ± 0.2	1.8 ± 0.2

The XRD diffraction patterns for the two prepared ceramic materials and the three sintering temperatures showed the presence of identical crystalline phases, metastable tricalcium phosphate (α-C$_3$P) and metastable wollastonite (α-CaSiO$_3$). XRD patterns for the optimized sintering temperature (1375 °C) are shown in Figure 1 as the representative.
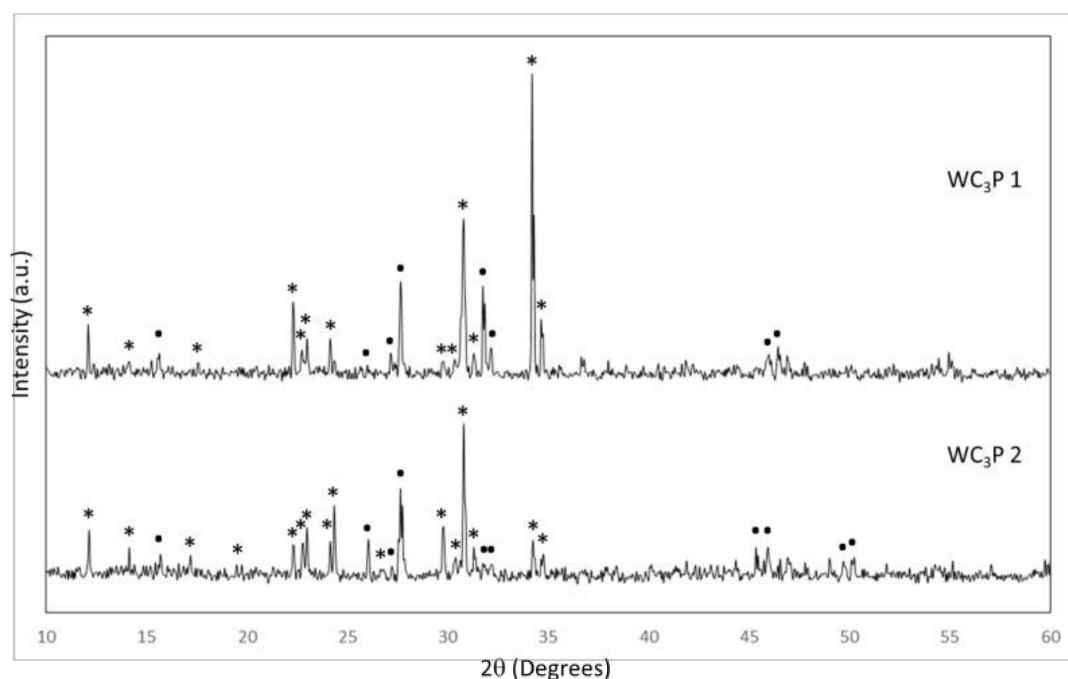

Figure 1. XRD pattern of synthesized ceramics W-C$_3$P 1 and W-C$_3$P 2 obtained at 1375 °C for 6 h. [(*) α-C$_3$P; (·) α-CaSiO$_3$].

The results of the confocal Raman microscopy studies performed on the samples are summarized in Figure 2. Figure 2a,c shows the optical micrograph images of the characteristic regions (150 μm × 150 μm) of samples W-C$_3$P 1 and W-C$_3$P 2, respectively. The Raman microscopy color profiles of the different phases identified in these regions are shown in Figure 2b,d. The average Raman spectra and the typical Raman spectra of the red- and blue-colored areas in the surface Raman images are presented in Figure 2d. These Raman spectra coincide for both samples.

The Raman spectra of the blue-colored areas only present the Raman bands that corresponded to the α-W phase [23,24]. At high frequencies, the three bands observed (Figure 2e) at 932, 985, and 1075 cm^{-1} represented mainly Si–O stretching modes. The mid-frequency bands at 511, 557, and 578 cm^{-1} were assigned to Si–O–Si bending and Si–O stretching modes, and the low wavenumber bands between 235 to 440 cm^{-1} corresponded to the silicate network deformation along with Ca–O stretching. The Raman spectra of the red-colored areas fitted the corresponding α-TCP phase very

well [25,26]. Spectra were characterized by the internal modes of vibrations of (PO_4^{3-}), the groups in the structure of this phase, ν_1 at 948, 969 cm^{-1}, ν_3 around 1080 cm^{-1}, ν_2 from 390–490 cm^{-1}, and ν_4 between 540–640 cm^{-1}, whereas the least intense band at 150–300 cm^{-1} was due to external lattice modes. Finally, a mixture of phases α-C$_3$P and α-W was identified in the average Raman spectra of the analyzed regions of both samples.
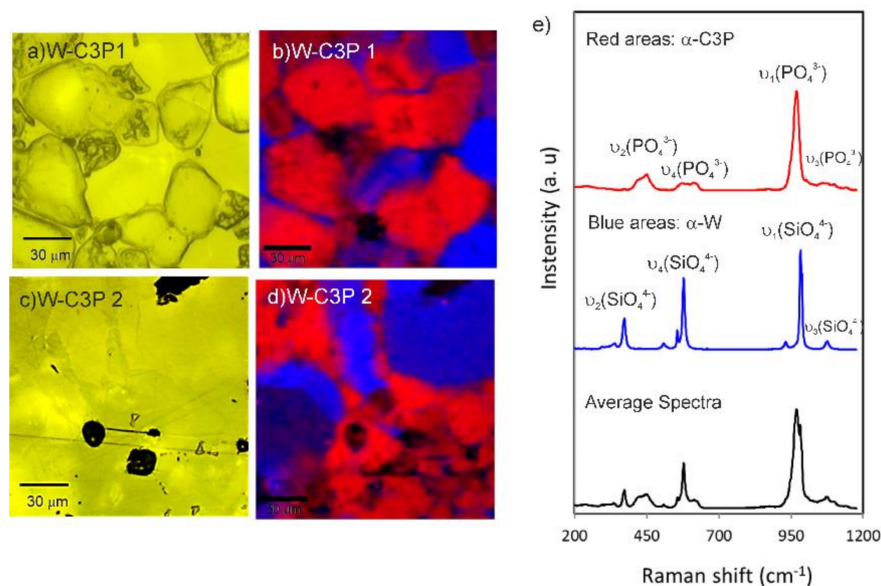
Figure 2. Optical micrographs of samples (**a**) WC$_3$P 1 and (**c**) WC$_3$P 2. Raman images representing the spatial phase distribution of phases α-CaSiO$_3$ and α-C$_3$P (blue and red regions) in samples (**b**) WC$_3$P 1 and (**d**) WC$_3$P 2. (**e**) Raman spectra associated with each region and the average spectra.

Figures 3 and 4 reveal the characteristic microstructural features of the WC$_3$P 2 sintered hypereutectic ceramic as being representative of both materials. The microstructure performed a homogeneous distribution of two kinds of areas with clearly different polished and chemical etching. The strongly etched zones gave a highly microcracked appearance and their composition could be attributed to α-C$_3$P. Next to these regions, uncracked α-W grains were observed, which were identified by the WDS microanalysis (Table 2). Porosity lowered from 1325 °C to 1375 °C, while pore size increased from ~16 μm at 1325 °C to ~44 μm at 1375 °C. The behavior was the same for both ceramics.
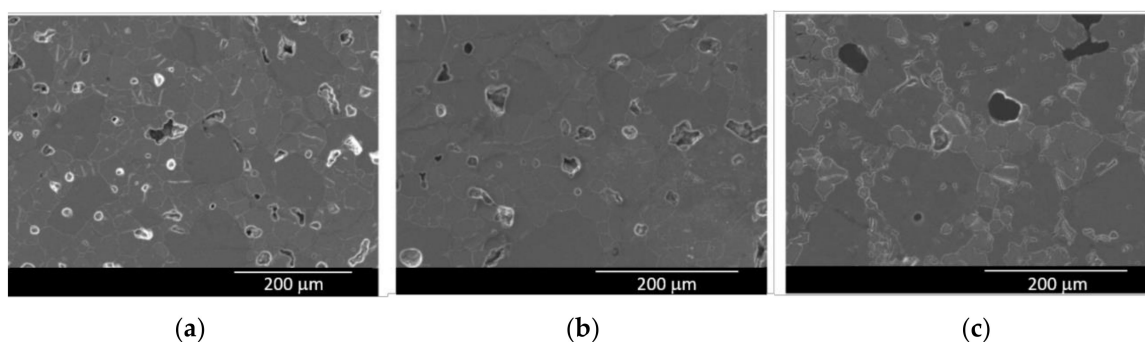

(**a**)   (**b**)   (**c**)

Figure 3. Surface SEM microphotographs of the W-C$_3$P 2 ceramic sintered for 6 h after polished and chemical etching, as representative of both ceramics at (**a**) 1325 °C, (**b**) 1350 °C, and (**c**) 1375 °C.
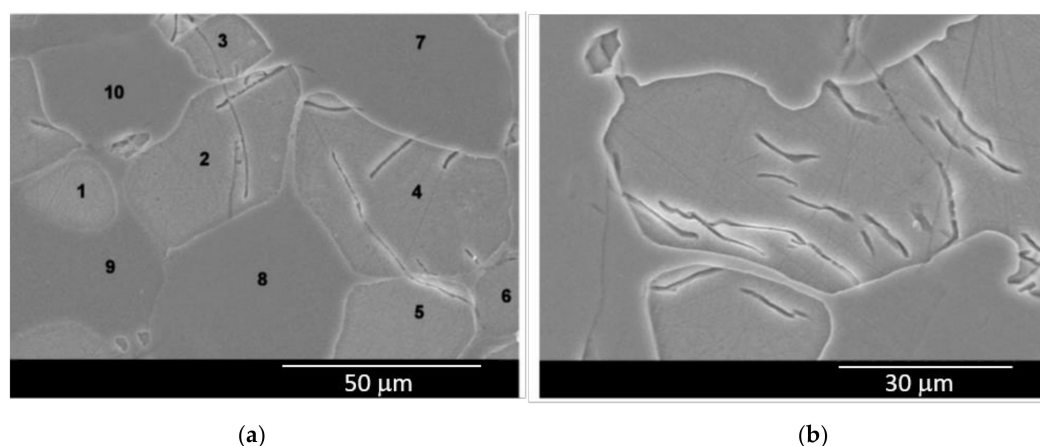
(**a**)　　　　　　　　　　　　　　　　　　(**b**)

Figure 4. SEM pictures of the WC_3P 1 sintered at 1375 °C for 6 h at (**a**) low magnification, showing the places where the WDS microanalysis of Table 2 were taken, and (**b**) high magnification of the C_3P grain for a detailed view of cracking.

Table 2. WDS analysis from Figure 4a.

Atomic %	1	2	3	4	5	6	7	8	9	10
	C_3P	C_3P	C_3P	C_3P	C_3P	C_3P	W	W	W	W
Si	0.95	1.15	0.80	1.01	1.19	0.99	48.84	49.07	49.24	49.16
P	38.86	38.96	38.17	37.95	37.96	38.64	0.04	0.08	0.23	0.12
Ca	60.19	59.89	61.03	61.04	60.85	60.37	51.12	50.85	50.53	50.72

Figure 4 shows a close-up microstructure for WC_3P 1 as the representative one, including dark gray grains of W (average size of ~67 ± 1 μm) and light gray grains of C_3P, with an average size ~26 ± 0.5 μm. In addition, several cracks (~14 μm long) are present in the C_3P grains. Presence of Si as a solid solution in C_3P, as well as P in the solid solution in grains W, were confirmed by the WDS results (Table 2). These results coincide with the phase diagram data, where the maximum solid solution of W in C_3P and that of C_3P in W at 1375 °C are 8 and 1.1 wt %, respectively, with the maximum solid solution at the invariant eutectic point (1402 ± 2 °C) of 10.2 and 1.5 wt %, respectively [27].

The Image J analysis was used for the volume fraction determination of each phase, with 68–69 ± 2 vol % for the light gray phase (dissolved phase) (C_3P) and 31–32 ± 2 vol % for the dark gray phase (W).

Acid chemical etching was used to develop the grain boundaries and different phases present in samples. By way of example, Figure 5 shows the topography of a 300×300 μm^2 typical area of the WC_3P 1 etched sample showing the 3D character of the surface. The surface evolves to an etched texture, which reflects the preferential dissolution of the C_3P phase. The roughness profiles of the sample surface were measured to quantitatively estimate this effect. The linear height profiles along lines 1, 2, and 3 (Figure 5a) are represented in Figure 5b–d, respectively. As a result of the etching process, a height difference of 1.5–2.5 μm between grains W and C_3P was measured. As expected, the grain boundaries were especially sensitive to the etching process and showed irregular and wide variations.

The ceramic sintered at 1375 °C had the lowest porosity and a high density. Therefore, this thermal treatment was selected as the best one and its ceramics were used for the in vitro bioactivity and cell behavior tests.

Diametrical compression test realized for WC3P 1 sintered at 1375 °C, as the representative one, showed that the greatest tensile strength was uniform across the central part of the diametrical plane of the specimens, as is shown in Figure 6a. Failure occurs through the diametrical plane and the specimens were broken in two similar pieces, which corresponds to a load drop in the load–displacement curve

registered during the test. The maximum load before the drop was used to calculate the diametrical strength, σf, using Equation (1) (Figure 6b).
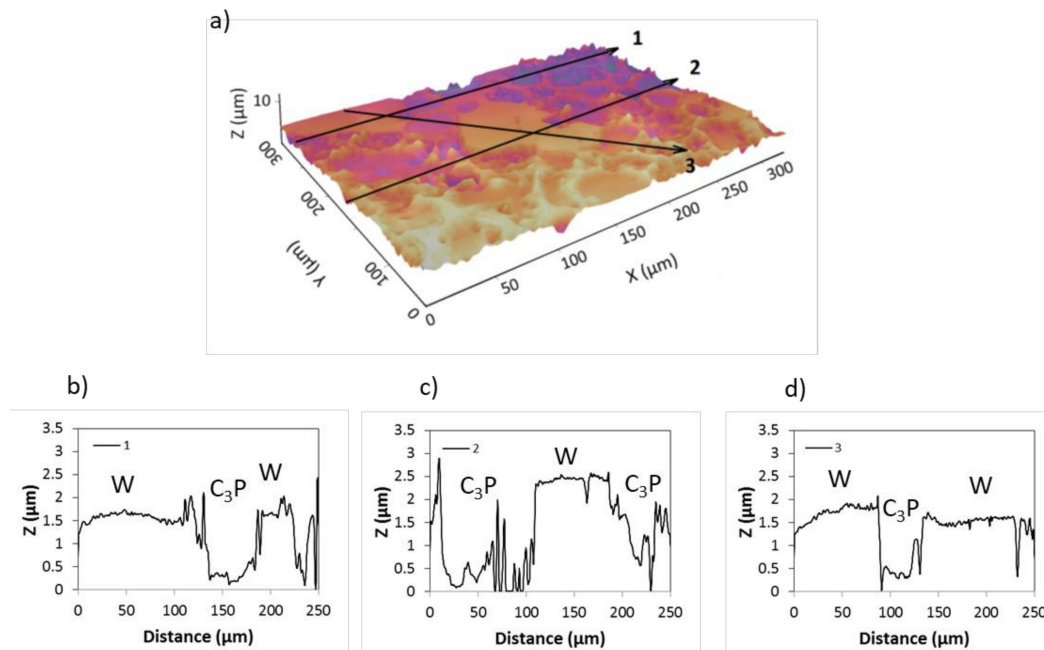

Figure 5. (**a**) 3D topographic image of the WC$_3$P 1 etched sample surface obtained by optical profilometry; (**b**–**d**) cross-section profile from lines 1, 2, and 3, respectively, taken from (**a**).
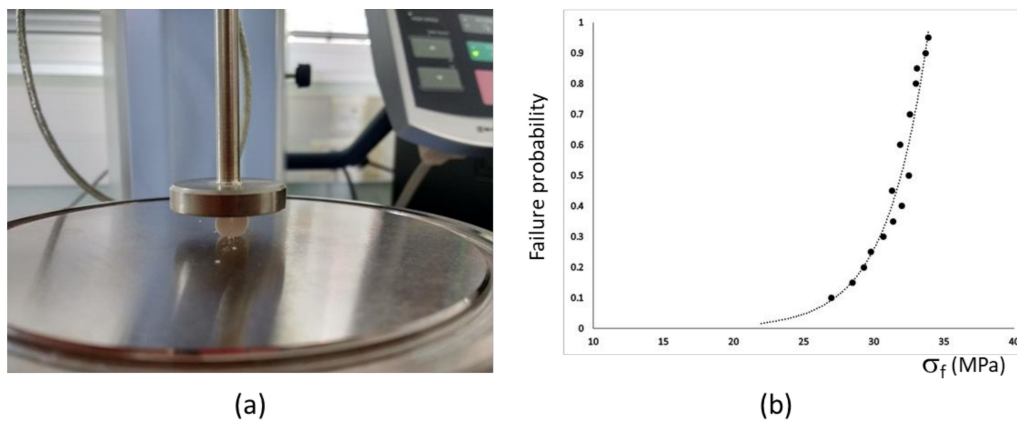

Figure 6. (**a**) Image of DCDT test and (**b**) Cumulative distribution for probability of failure versus diametrical compression strength for WC$_3$P 1.

According to the DCDT test, the greatest mechanical strength was 32.5 MPa, which is in agreement with previous values found in the literature for wollastonite-based materials [28].

3.2. In Vitro Bioactivity

Figure 7 shows the characteristics of the ceramic surface after SBF soaking for several periods of time. At the beginning of the test, the dissolution of the grain boundaries was observed in both ceramics (Figure 7a). After three days of testing, a discontinuous layer of the fine precipitate (with no definite shape) was viewed on the surface of both ceramics with some nano-sized aggregates (Figure 7b). As the test continued, the precipitate became a continuous layer that covered the entire surface of both materials after one week of testing and acquired a globular morphology (Figure 7c). Its grain size increased with time.
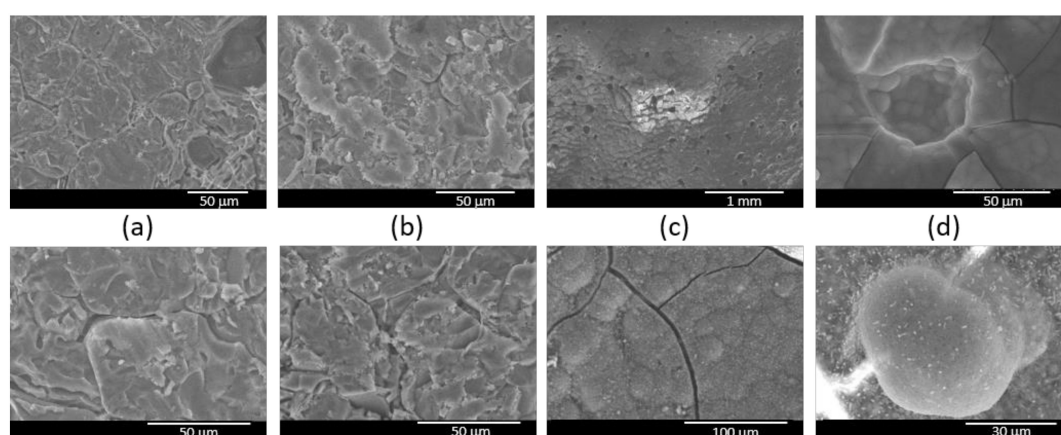
Figure 7. SEM images of WC$_3$P 1 (top) and WC$_3$P 2 (down) as being representative of the soaking times in SBF of (**a**) one day, (**b**) three days (**c**) one week, and (**d**) four weeks.

This new precipitate layer was different in both ceramics. While the new layer in ceramic WC$_3$P 1 had pores all over its surface (Figure 7c top), the globular new phase in ceramic WC$_3$P 2 grew to form a compact and continuous layer with no pores, and visible cracks were even observed due to the drying process it was submitted to while preparing it for the SEM analysis.

At four weeks, no differences were observed with the layer formed in the first week. Figure 7d shows details of a pore (average ~43 μm) on the surface of the precipitate in WC$_3$P 1 and details of the globular morphology (average ~58 μm in ⌀) from WC$_3$P 2. This precipitate was identified in both ceramics as being composed of calcium and phosphorus by the WDS analysis, with Ca/P ratios of about ~1.65 ± 0.04.

Figures 8 and 9 show the polished cross-section at weeks 1 and 4 as being representative for the study period, and its relevant X-ray maps for calcium, phosphorus, and silicon elements by revealing the microstructure of both ceramics–SBF interfaces. For these periods, an increase in precipitated layer thickness according to that observed by SEM went from 4.41 to 14.62 μm for WC$_3$P 1 (Figure 8) and from 7.67 to 17.55 μm for WC$_3$P 2 (Figure 9). This outer layer was composed of a Ca/P rich phase with Ca/P ratios of about ~1.65–1.68, while a fine underlayer in direct contact with the substrate was observed, more evident for WC$_3$P 2 after four weeks of soaking, rich in silicon. The crack seen in the figure between the precipitated outer layer and the ceramic is an artefact caused by the polishing of the specimen.
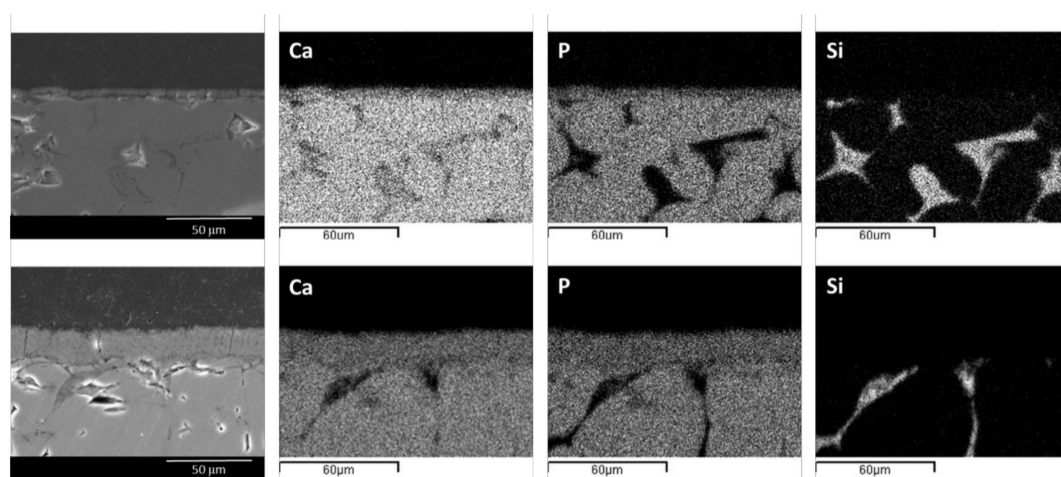

Figure 8. Mapping for WC$_3$P 1 after one week of soaking (upper image) and four weeks of soaking (bottom image) in SBF.
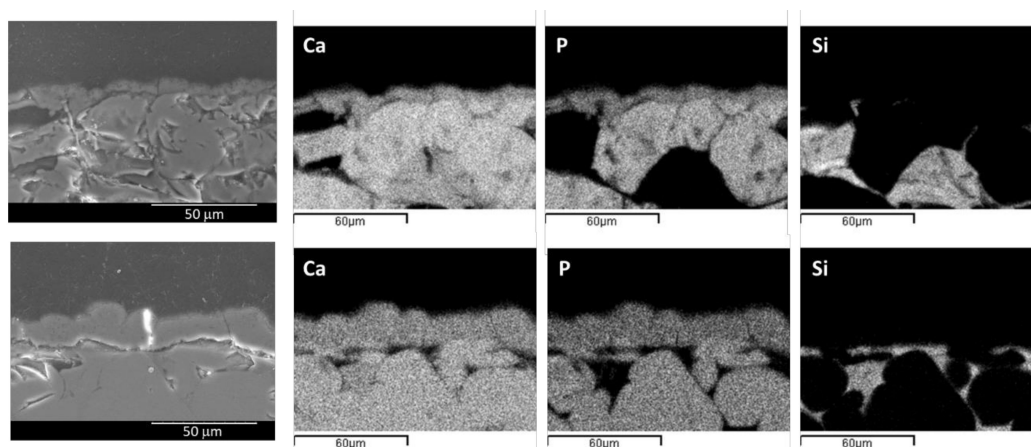
Figure 9. Mapping for WC$_3$P 2 after one week of soaking (upper image) and four weeks of soaking (bottom image) in SBF.

The experimental changes in the calcium, phosphorus, and silicon ion concentrations of SBF measured by the ICP technique on different soaking days are shown in Figure 10. The composition of the original SBF solution is also included in the figure as the 0 days soaking time.
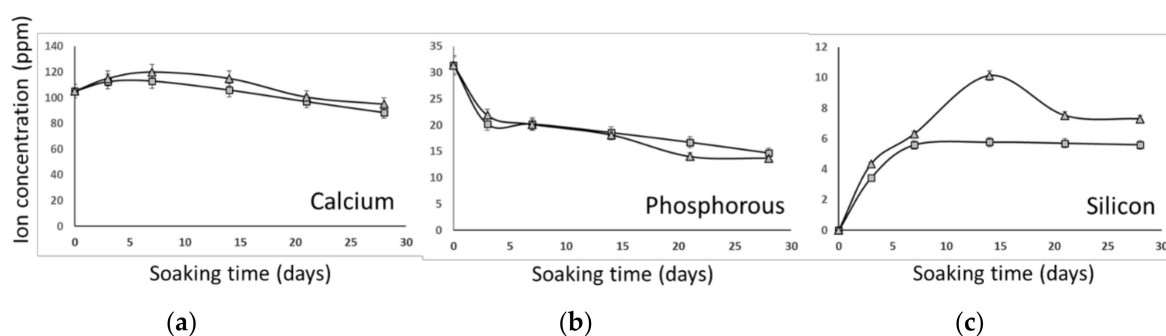

| (a) | (b) | (c) |

Figure 10. Changes in the (**a**) calcium, (**b**) phosphorus, and (**c**) silicon ion concentrations with soaking in SBF solution for (■) WC$_3$P 1 and (▲) WC$_3$P 2.

A sudden improvement in the Ca and Si ion concentrations was observed for the first three days of the study, whereas the P ions decreased throughout the test. The main difference is related to Si. For both ceramics, the silicon ion showed a rapid increase in the first week after which a different behavior was seen: a continuous release for WC$_3$P 1, and a reduction over time for WC$_3$P 2 after a peak at 14 days.

In the next part of the study, high-resolution transmission electron microscopy (HRTEM) was used to analyze the ultrastructure of the surface product that formed after the longest exposure time (Figure 11). The TEM results discovered a precipitate formed by nanocrystal (Figure 11a), composed mainly of Ca and P (data not shown). As is shown in Figure 11b, measured lattice spacing values are in agreement with those found in the literature for carbohydroxyapatite (CHA) [29–31]. When the specimens were appropriately oriented, the SAD often displayed (002) and (211) arcs, which indicates the preferential orientation of the CHA crystals on the layer (interior of Figure 11a,b). The HRTEM and SAD results were compared with information for the B-type CHA in JCPDS (#19-272) [32], which confirmed the preferential orientation of CHA crystallites in the surface product. A slight deviation of the d spacing from the standard CHA was observed because Si impurities may be incorporated into the CHA structure. In Figure 11c, the presence of an amorphous phase is observed in the WC$_3$P 2 ceramic.
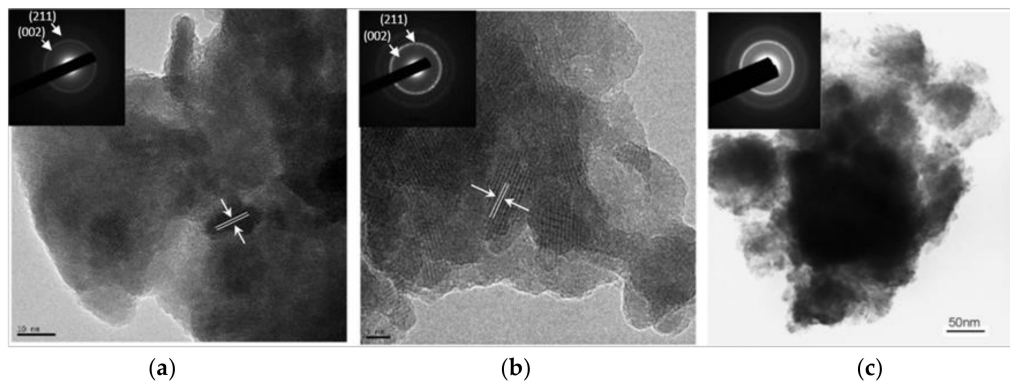
(a)   (b)   (c)

Figure 11. TEM, HRTEM, and SAD micrographs of the precipitated layer after immersion in SBF of four weeks, (**a**) WC$_3$P 1 and (**b**) WC$_3$P 2 surface product, (**c**) the amorphous product of WC$_3$P 2.

3.3. Cellular Adhesion, Morphology, and Proliferation Assays

Biocompatibility studies were carried out on WC$_3$P 2 using the isolated *ah*MSCs. Figure 12 shows the growth and expansion of *ah*MSCs after 1, 7, 14, 21, and 28 days of incubation in GM.
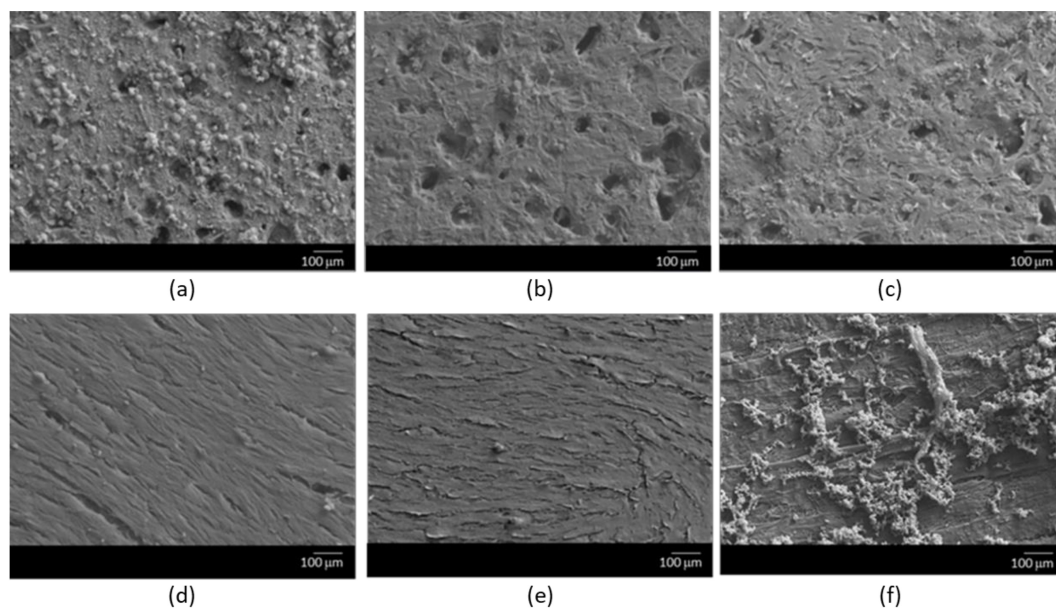

(a)   (b)   (c)

(d)   (e)   (f)

Figure 12. FESEM images showing the growth of *ah*MSCs on the WC$_3$P 2 ceramic surface after (**a**) 1 day, (**b**) 7 days, (**c**) 14 days, (**d**) 21 days, and (**e**,**f**) 28 days in GM.

After the first 24 h of culture (Figure 12a), the ceramic surface exhibited a granular layer with some spicules and small nodules, which corresponded to a Ca–P deposit according to the microanalysis by SEM-EDX observations (data not shown), covering part of it. Cells seemed to have adapted quickly as their adhesion was enhanced by spreading of cytoplasmic digitations across the surface of the material, increasing contact area. From 7 to 14 days of incubation (Figure 12b,c), the number of cells was increased and started to form connections with one another. However, the largest number of cells was observed after 21 and 28 days of incubation (Figure 12d,e). The *ah*MSCs began to form a continuous monolayer with fibroblast growth, exhibited as a flattened and spreading morphology. Cells showed good development and proliferation on the surface's material. Finally, in Figure 12f, we can see the formation of a fibrillary network, formed by extracellular components, occupying intercellular gaps, which started to appear after 21 days of incubation.

Throughout the study, there were no signs of cytotoxicity or morphological alterations while cells grew and spread on the material.

The Alamar Blue assay aimed to quantitatively measure cell proliferation, directly on the W-C_3P 2 ceramic's surface and was again the representative one. Figure 13 shows the results obtained on the ceramic materials compared to the positive controls (cells seeded on TCPS).
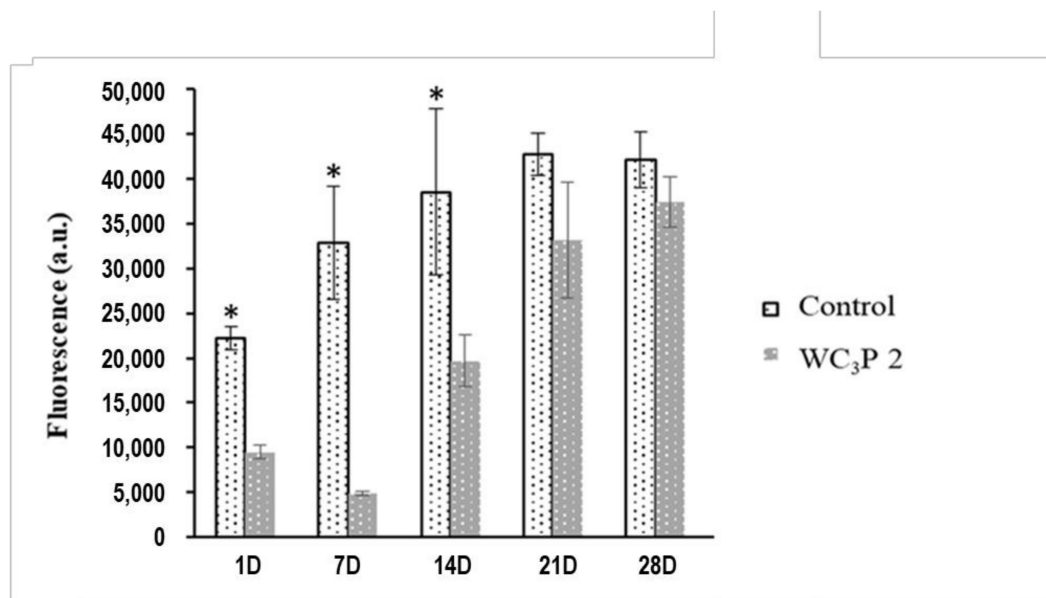

Figure 13. The Alamar Blue assay showing cellular metabolic activity of cells after seeding on the WC$_3$P 2 scaffolds and the positive control (in plastic) as a comparative reference. Significant difference ($p < 0.05$) between cells on the bioceramic's surface and the positive control at identical experimental times denoted as *.

Fluorescence, in arbitrary units (a.u.), is represented graphically versus cells' incubation times, and it increased gradually in both cases, which indicates good viability and proliferation rates.

Less metabolic activity was observed for the *ah*MSCs cultured on the ceramics from the positive control at all the studied times, but no significant differences between them were observed from 21 days of incubation. For the cells seeded on plastic (positive control), the maximum metabolic activity value was constant from day 21.

4. Discussion

In agreement with information on the pseudobinary system $Ca_3(PO_4)_2$-$CaSiO_3$ [27], the phases formed at room temperature would be β-C_3P and wollastosnite-2M. However, the studied biphasic ceramic was constituted by two metastable crystalline phases as determined by XRD (Figure 1), a SEM-WDS microanalysis (Table 2), and μ-Raman (Figure 2), namely, α-wollastonite and α-tricalcium phosphate. This discrepancy between the phases found in the real materials, and those in the thermodynamic equilibrium, can be explained by the kinetic effects on high-temperature reactions and transformations during cooling. Some authors have reported that small quantities of Si in C_3P could stabilize the high-temperature form of C_3P [33,34].

Both ceramics showed significantly increased shrinkage at 1350 °C (Table 1) while sintering the green compacts, which can be explained by the existence of a liquid phase. In the materials with certain quantities of impurities, a liquid phase can form at temperatures lower than those of the equilibrium of pure materials [35]. With WC$_3$P 1 and WC$_3$P 2, liquid might appear at temperatures as low as 1402 °C (invariant eutectic temperature of the pseudobinary system). As checked, the density of the ceramics sintered at 1375 °C was considerably higher than that of those sintered at 1350 °C, which is consistent

with the presence of a glass phase. In any case, the amount of liquid formed at 1375 °C (slightly below the eutectic temperature) was so small that its presence in the microstructure of both ceramics was not detected, in which the grain boundaries between phases $CaSiO_3$ and $Ca_3(PO_4)_2$ were conventional and no other secondary phases could be related with liquid (Figures 3 and 4).

The swallowing of the WC_3P 2 ceramic sintered at 1375 °C shown in Figure 3c could be due to the formation of a low-viscosity calcium-silicophosphate liquid that penetrated open pores by capillarity, which led to their closing as observed by the large round pores presented in the microstructure.

The enhanced ceramic was that sintered at 1375 °C, which presented a homogeneous microstructure that consisted in phases α-W and α-C_3P. The α-C_3P grains presented microcracks through grains (Figure 3a) and with a larger quantity in ceramic WC_3P 2 with a bigger wollastonite grain size (Figure 3b).

The cause of the microcracks observed in both ceramics sintered at 1375 °C could be due to the stresses generated by the difference in the thermal expansion coefficient between α-W (10×10^{-6} K^{-1}) and α-C_3P (60×10^{-6} K^{-1}) [36–38] and/or by the crystalline anisotropy of both phases. Fine microstructures would limit cracking because the critical cracking size could not be achieved. Cracks would form for the grains larger than the critical size (Figure 3).

Diametrical compression test realized for WC_3P 1 as the representative one (Figure 6) showed 32.5 MPa as the greatest strength value. Additional mechanical studies are in progress, but this result is promising for getting adequate mechanical support during bone regeneration in our future research goal: sinus lift procedures.

The ions measured by ICP from the SBF medium was done to control the possible ion release, which would occur in vivo and attempt to clarify the bioactivity mechanism. The concentration of the different ions present in SBF throughout the experimental time (Figure 10) showed differences that could be attributed to the wollastonite particle size. For the *in vitro* analysis by immersion in SBF, both ceramics displayed increased calcium and silicon ion concentrations during the first week of the experiment, which indicated the partial surface dissolution of the α-W phase. The degradation rate of a material in a living body should equal the bone tissue repair process for bone regeneration applications. In addition, the precipitate layer of apatite over the material is usually considered a sign of bioactivity, which was studied in-depth in this research study. The α-W phase showed a significantly higher dissolution rate than the α-C_3P (Figure 10) like the SBF enriched in the Si ion. These processes occurred initially on the grain boundaries; subsequently, the diffusion process occurred intergranularly, and porosity was sometimes generated in the material in the first process stages (Figure 7). This might be due to the constant solubility product of α-W ($2.53 \ 10^{-8}$) being much bigger than that of α-C_3P (2.03×10^{-29}) [39], which suggests a faster dissolution rate for the α-W phase. Behavior was slightly different in both ceramics: after four weeks, the presence of an amorphous silica phase prior to precipitate deposition was especially visible for sample WC_3P 2 (Figure 9 bottom, and Figure 11c). The presence of the amorphous silica layer, as reported in the scientific literature for such reactions [35], was not detected in the SEM/WDS cross-section studies of WC_3P 1 (Figure 8). This would explain the depletion of the Si ion in the SBF of WC_3P 2 at two weeks. It remained in the form of amorphous Si on the ceramic surface, whereas all the Si ions in WC_3P 1 passed to the medium, and no maximum value was reached during the experiment.

When analyzing P ion evolution, both ceramics showed a gradual decrease throughout the assay. This was probably due to the reaction of α-C_3P with calcium and hydroxyl ions at the medium, which became HA according to the following: $3(Ca_3(PO_4)_2) + Ca + 2OH \rightarrow Ca_{10}(PO_4)_6(OH)_2$. As no increase in Ca had taken place after the first week, most Ca had to react with P at the interface, which would lead to the nucleation on the surface of the Ca–P powder particles (Figure 7b), which transformed into a new Ca–P rich layer with time.

In the second immersion stage, a globular layer, which almost covered the entire surface, was observed for both ceramics (Figure 7) as a Ca–P rich layer. This precipitate grew with exposure time (Figures 8 and 9) and developed a continuous layer, which, with WC_3P 1, presented porosity

(Figure 7c (upper) and Figure 8). Thickness was measured from one to four weeks (representative periods) with values of 14.62 μm for WC$_3$P 1 and 17.55 μm for WC$_3$P 2 (Figures 8 and 9, respectively). The thickness data represent the average of 10 independent determinations. It was possible to control the dissolution of the bioceramic by adjusting the raw particle size of α-W. However, more in vivo degradation studies must be conducted to confirm the changes noted in the degradation properties of the WC$_3$P bioceramics.

These preliminary studies have shown that both cell viability and biocompatibility were good [40]. However, it is necessary to do more assays to confirm this. Ions released from bioceramics, like calcium, silicon, and phosphate groups, can determine cell functions, such as adhesion and proliferation.

The FESEM images and alamarBlue results showed the biomaterials' good biocompatibility. Between day 1 and 7, the number of cells was small and metabolic activity was low. This could be explained by the self-renewal capacity of *ah*MSCs, which is related to their growth and proliferation properties. The bioceramic surface is a new environment for cells, which need some time to adapt to it. However, metabolic activity and the number of the cells increased from day 14 until the end of the study time, when cells occupied the whole biomaterial's surface.

With respect to the limitations of the experiment for obtaining a material with open porosity, it was observed that one of the constituent phases of the material (W) was not completely dissolved, because of which our starting hypothesis was not fulfilled. We are currently working on a new experimental design which will change the composition allowing wollastonite to be the major phase and a heat treatment that will favor nucleation but not growth, for a more homogeneous distribution of this phase that allows smaller grains of Wollastonite to be generated, but grains large enough for cell colonization.

5. Conclusions

In this study, dense WC$_3$P (30–70 wt %) ceramics were successfully prepared by sintering WC$_3$P powder with different particle size ratios at 1375 °C for 6 h. The obtained ceramic presented a homogeneous biphasic microstructure that included grains from a resorbable phase, α-W (30 wt %, and 63–100 μm or 100–150 μm), and another corresponding to α-C$_3$P (70 wt %, ~30 μm) that pseudomorphically transformed into a HA-like formation. Thermal expansion led to the microcracking of the α-C$_3$P phase in the ceramic while cooling down from the sintering temperature.

Immersion in SBF allowed a globular apatite layer to develop on its surface. Apatite formation took place through the dissolution of the α-W phase with subsequent transformation of α-C$_3$P into HA. After nucleation, HA growth developed a similar layer to bone-like apatite on its surface.

Although both ceramics presented *in vitro* bioactivity and cellular biocompatibility, our initial hypothesis about open porosity formation by complete α-W dissolution was not fulfilled. It is known that ceramics with an α-W phase of a larger grain size dissolve more quickly.

The *in vitro* cell culture experiments showed good morphology, adhesion, and proliferation of *ah*MSCs on the WC$_3$P ceramics. It would be necessary to analyze the in vivo response of this biomaterial, because of the limitations in the *in vitro* tests. Nonetheless, the obtained results were sufficient to lead us to believe that it could act as an effective scaffold for bone tissue engineering.

More in vivo degradation studies must be conducted to confirm the changes in degradation properties of the W-C$_3$P bioceramics, and as well a comprehensive mechanical study comparing our scaffold with a dense material.

Author Contributions: P.M. performed the preparation and characterization of ceramic material and the bioactivity in vitro study. P.R.-T. performed the biocompatibility and viability assays. S.S. performed the Raman and topographic studies. P.M., L.M.-O., and P.A. were responsible for designing, analyzing, and discussing results, and, finally, P.M. and P.A. were involved in the manuscript preparation.

Conflicts of Interest: The authors declare no conflict of interest.

References

1. Dorozhkin, S.V. Calcium orthophosphate bioceramics. *Ceram. Int.* **2015**, *41*, 13913–13966. [CrossRef]
2. Islam, M.T.; Felfel, R.M.; Abou Neel, E.A.; Grant, D.M.; Ahmed, I.; Hossain, K.M.Z. Bioactive calcium phosphate–based glasses and ceramics and their biomedical applications: A review. *J. Tissue Eng.* **2017**, *8*, 1–16. [CrossRef] [PubMed]
3. De la Casa-Lillo, M.A.; Velasquez, P.; De Aza, P.N. Influence of thermal treatment on the "in vitro" bioactivity of wollastonite materials. *J. Mater. Sci: Mater. Med.* **2011**, *22*, 907–915. [CrossRef] [PubMed]
4. Dashnyam, K.D.; Ahmed, E.-F.; Buitrago, J.O.; Pérez, R.A.; Knowles, J.C. ; Kim, H-W. A mini review focused on the proangiogenic role of silicate ions released from silicon-containing biomaterials. *J. Tissue. Eng.* **2017**, *8*, 1–13. [CrossRef] [PubMed]
5. Eliaz, N.; Metoki, N. Calcium phosphate bioceramics: A review of their history, structure, properties, coating technologies and biomedical applications. *Materials* **2017**, *3*, 334. [CrossRef] [PubMed]
6. Ros-Tárraga, P.; Mazón, P.; Rodríguez, M.A.; Meseguer-Olmo, L.; De Aza, P.N. Novel resorbable and osteoconductive calcium silicophosphate scaffold induced bone formation. *Materials* **2016**, *9*, 785. [CrossRef] [PubMed]
7. Mazón, P.; De Aza, P.N. Porous scaffold prepared from α'_L-dicalcium silicate doped with phosphorus for bone grafts. *Ceram. Int.* **2018**, *44*, 537–545. [CrossRef]
8. Baino, F.; Caddeo, S.; Novajra, G.; Vitale-Brovarone, C. Using porous bioceramic scaffolds to model healthy and osteoporotic bone. *J. Eur. Ceram. Soc.* **2016**, *36*, 2175–2182. [CrossRef]
9. Shao, H.F.; He, Y.; Fu, J.Z.; He, D.S.; Yang, X.Y.; Xie, J.J.; Ya, C.L.; Ye, J.; Xu, S.Z.; Gou, Z.R. 3D printing magnesium-doped wollastonite/beta-TCP bioceramics scaffolds with high strength and adjustable degradation. *J. Eur. Ceram. Soc.* **2016**, *36*, 1495–1503. [CrossRef]
10. Itala, A.I.; Ylanen, H.O.; Ekholm, C.; Karlsson, K.H.; Aro, H.T. Pore diameter of more than 100 m is not requisite for bone ingrowth in rabbits. *J. Biomed. Mat. Res.* **2001**, *58*, 679–683. [CrossRef]
11. Karageorgiou, V.; Kaplan, D. Porosity of 3D biomaterial scaffolds and osteogenesis. *Biomaterials* **2005**, *26*, 5475–5491. [CrossRef] [PubMed]
12. Pérez, R.A.; Mestres, G. Role of pore size and morphology in musculo-eskeletal tissue engine. *Mat. Sci. Eng. C* **2016**, *61*, 922–939. [CrossRef] [PubMed]
13. De Aza, P.N.; Guitian, F.; De Aza, S. A new bioactive material, which transforms in situ into hydroxyapatite. *Acta Mater.* **1998**, *46*, 2541–2549. [CrossRef]
14. De Aza, A.H.; Velásquez, P.; Alemany, M.I.; Pena, P.; De Aza, P.N. In situ bone-like apatite formation from a bioeutectic®ceramic in SBF dynamic flow. *J. Am. Ceram. Soc.* **2007**, *90*, 1200–1207. [CrossRef]
15. De Aza, P.N.; Peña, J.I.; Luklinska, Z.B.; Meseguer-Olmo, L. Bioeutectic® ceramics for biomedical application obtained by laser floating zone method. In vivo evaluation. *Materials* **2014**, *7*, 2345–2410. [CrossRef] [PubMed]
16. Ni, S.; Chang, J.; Chou, L.; Zhai, W. Comparison of osteoblast-like cell responses to calcium silicate and tricalcium phosphate ceramics in vitro. *J. Biomed. Mater. Res. B Appl. Biomater.* **2007**, *80*, 174–183. [CrossRef] [PubMed]
17. De Aza, P.N.; Guitian, F.; De Aza, S.; Valle, F.J. Analytical control of wollastonite for biomedical applications by use of atomic absorption spectrometry and inductively coupled plasma atomic emission spectrometry. *Analyst* **1998**, *123*, 681–685. [CrossRef] [PubMed]
18. Magallanes-Perdomo, M.; Pena, P.; De Aza, P.N.; Carrodeguas, R.G.; Rodríguez, M.A.; Turrillas, X.; De Aza, S.; De Aza, P.N. Devitrification studies of wollastonite-tricalcium phosphate eutectic glass. *Acta Biomater.* **2009**, *5*, 3057–3066. [CrossRef]
19. Weibull, W. A statistical distribution function of wide applicability. *J. Appl. Mech.* **1951**, *18*, 292–297.
20. Kokubo, T.; Takadama, H. How useful is SBF in predicting in vivo bone bioactivity? *Biomaterials* **2006**, *27*, 2907–2915. [CrossRef]
21. Meseguer-Olmo, L.; Aznar-Cervantes, S.; Mazón, P.; De Aza, P.N. In vitro behavior of adult mesenchymal stem cells of human bone marrow origin seeded on a novel bioactive ceramics in the Ca_2SiO_4-$Ca_3(PO_4)_2$ system. *J. Mater. Sci: Mater. Med.* **2012**, *23*, 3003–30014. [CrossRef]
22. Dominici, M.; Le Blanc, K.; Mueller, I.; Slaper-Cortenbach, I.; Marini, F.; Krause, D.; Deans, R.; Keating, A.; Prockop, D.; Horwitz, E. Minimal criteria for defining multipotent mesenchymal stromal cells. The international society for cellular therapy position statement. *Cytotherapy* **2006**, *8*, 315–317. [CrossRef] [PubMed]

23. Richet, P.; Mysen, B.O.; Ingrin, J. High-temperature X-ray diffraction and raman spectroscopy, of diopside and pseudowollastonite. *Phys. Chem. Miner.* **1998**, *25*, 401–414. [CrossRef]

24. Pešková, Š.; Machovič, V.; Procházka, P. Raman spectroscopy structural study of fired concrete. *Ceram. Silik.* **2011**, *55*, 410–417.

25. De Aza, P.N.; Santos, C.; Pazo, A.; De Aza, S.; Cusco, R.; Artus, L. Vibrational properties of calcium phosphate compounds 1. Raman spectrum of α-tricalcium phosphate. *Chem. Mater.* **1997**, *9*, 912–915. [CrossRef]

26. Jillavenkatesa, A.; Condrate, R.A. The infrared and Raman spectra of β-and α-tricalcium phosphate ($Ca_3(PO_4)_2$). *Spectrosc. Lett.* **1998**, *31*, 1619–1634. [CrossRef]

27. De Aza, P.N.; Guitian, F.; De Aza, S. Phase-Diagram of wollastonite-tricalcium phosphate *J. Am. Ceram. Soc.* **1995**, *78*, 1653–1656. [CrossRef]

28. Carrodeguas, R.G.; De Aza, A.H.; De Aza, P.N.; Baudín, C.; Jiménez, J.; López-Bravo, A.; Pena, P.; De Aza, S. Assesment of natural and synthetic wollasonite as source for bioceramics preparation. *J. Biomed. Mat. Res. Part. A* **2007**, *83*, 484–495. [CrossRef]

29. Spector, M. High-resolution electron-microscope study of lattice images in biological apatites, *J. Microsc.* **1975**, *103*, 55–62. [CrossRef]

30. De Aza, P.N.; Luklinska, Z.B.; Anseau, M.; Guitian, F.; De Aza, S. Electron microscopy of interfaces in a wollastonite-tricalcium phosphate Bioeutectic. *J. Microsc.* **1998**, *189*, 145–153. [CrossRef]

31. Kerebel, B.; Daculsi, G.; Verbaere, A. High-resolution electron-microscopy and crystallographic study of some biological apatites. *J. Ultrastruct. Res.* **1976**, *57*, 266–275. [CrossRef]

32. Minarelli-Gaspar, A.M.; Saska, S.; Da Cunha, L.R.; Bolini, P.D.A.; Carrodeguas, R.G.; De Aza, A.H.; Pena, P.; De Aza, P.N.; De Aza, S. Comparison of the biological behavior of wollastonite bioceramics prepared from synthetic and natural precursors. *Key Eng. Mater.* **2008**, *361–363*, 1083–1086.

33. Martínez, I.; Velásquez, P.; Meseguer-Olmo, L.; De Aza, P.N. Production and study of in vitro behavior of monolithic α-tricalcium phosphate based ceramics in the system $Ca_3(PO_4)_2$–Ca_2SiO_4. *Ceram. Int.* **2011**, *37*, 2527–2535. [CrossRef]

34. Velásquez, P.; Luklinska, Z.B.; Meseguer-Olmo, L.; Mate-Sánchez de Val, J.E.; Delgado-Ruíz, R.A.; Calvo-Guirado, J.L.; Ramírez-Fernández, M.P.; De Aza, P.N. αTCP ceramic doped with dicalcium silicate for bone regeneration applications prepared by powder metallurgy method: In vitro and in vivo studies. *J. Biomed. Mater. Res. Part A* **2013**, *101*, 1943–1954. [CrossRef] [PubMed]

35. Alemany, M.I.; Velásquez, P.; De la Casa-Lillo, M.A.; De Aza, P.N. Effect of materials' processing methods on the in vitro bioactivity of wollastonite glass-ceramic materials *J. Non-Cryst. Sol.* **2005**, *351*, 1716–1726. [CrossRef]

36. Carrodeguas, R.G.; De Aza, A.H.; Jimenez, J.; De Aza, P.N.; Pena, P.; López-Bravo, A.; De Aza, S. Preparation and in vitro characterization of wollastonite doped tricalcium phosphate bioceramics. *Key Eng. Mater.* **2008**, *361–363*, 237–240.

37. Bauer, G.; Hohenberger, G. Causes of behavioral variation of bioactive calcium phosphate ceramics in living organism. *Ber. Dtsch. Chem. Ges.* **1989**, *66*, 23–27.

38. Ibáñez, A. Síntesis de Wollastonita a Partir de Diatomitas Españolas y Estudio de su Aplicación en Revestimientos Cerámicos Porosos Procesados por Cocción Rápida. Ph.D. Thesis, Universidad Autónoma de Madrid, Madrid, Spain, 1993.

39. Black, J.; Hastings, G. *Handbook of Biomaterials Properties*; Champan & Hall: Boca Raton, Fl, USA, 1998.

40. Mazón, P.; García-Bernal, D.; Meseguer-Olmo, L.; Cragnolini, F.; De Aza, P.N. Human mesenchymal stem cell viability, proliferation and differentiation potential in response to ceramic chemistry and surface roughness. *Ceram. Int.* **2015**, *44*, 6631–6644. [CrossRef]